Power Scalable TEM$_{OO}$ CW Nd:YAG Laser with Thermal Lens Compensation

D. Mudge, M. Ostermeyer, P. J. Veitch, J. Munch, *Member, IEEE*, B. Middlemiss, D. J. Ottaway, and M. W. Hamilton

Abstract—We present finite-element analyzes and experimental results to validate our approach for building high-power single-mode Nd:YAG lasers. We show that the thermooptical and thermomechanical properties of a slab laser can be controlled. This is essential for the use of the proposed unstable resonator. We include demonstration of an efficient subscale laser operating at 20 W TEM$_{oo}$.

Index Terms—CW lasers, laser measurements, laser resonators, laser thermal factors, neodymium:YAG lasers, semiconductor lasers, thermal variables control, thermal variables measurement.

I. INTRODUCTION

HIGH-POWER, diode-laser-pumped continuous-wave (CW) solid-state lasers with excellent beam quality are required in various industrial, military, medical, and scientific applications. One of the most demanding applications is the laser source for the interferometric detection of gravitational waves [1], [2]. Here an output greater than 100 W in a single frequency and near diffraction-limited beam quality is required at 1 μm. Previous attempts to achieve this goal have been limited by degradations in efficiency and beam quality by thermal lensing, stress-induced birefringence, and thermal aberrations. In this paper, we shall review some of these issues and describe our laser architecture approach and current results for efficient production of diffraction-limited beams at high powers [3].

Efficient CW operation of diode-laser end-pumped side-cooled rod lasers is possible due to the good spatial overlap of the pump light and the fundamental laser mode. Tidwell *et al.* [4] reported a near-diffraction-limited TEM$_{oo}$ output power of 60 W with an optical efficiency of 26% from a Nd:YAG laser that used two rods, each of which were pumped at both ends. However, the thermal fracture strength of the gain medium limits the pump density at the end face [5], and thus multiple end-pumped rods would be required to produce higher powers.

Side-pumping of a laser rod allows a greater amount of pump power to be deposited within the gain medium. Golla *et al.* [6] have demonstrated a TEM$_{oo}$ output power of 62 W with an efficiency of 17%. The decrease in efficiency is due to poor extraction of the energy near the edges of the rod by the fundamental mode as well as thermally induced birefringence effects and lensing within the laser rod. The maximum TEM$_{oo}$ output

power is expected to be limited to 100–150 W with decreasing efficiency for a single-rod laser.

A well-known solution that significantly reduces thermal lensing, stress-induced biaxial focusing, and birefringence is the side-pumped, side-cooled zigzag slab laser [7]. The rectilinear geometry reduces the problems associated with stress-induced birefringence and the zigzag optical path minimizes thermal and stress-induced focusing. Furthermore, the zigzag optical path allows extraction of energy from the edges of the slab where the pump density is greatest. Finally, coplanar pumping and heat removal permit increasing the power of the laser simply by increasing the height of the pumped region. The zigzag optical path and side-pumped, side-cooled slab is the basis of many high-power solid-state laser designs [3], [8]–[10].

In practice, a finite-height slab will have a thermal lens in the (vertical) plane normal to the zigzag, which can compromise gain extraction and mode control. In this paper, we shall describe a design that solves this problem by incorporating active temperature control of the bottom and top surfaces of the slab, allowing adjustment of the thermal lens [9]. We present interferometric evidence to demonstrate detailed control of the vertical thermal lens and confirm the absence of a strong or variable thermal lens in the horizontal zigzag plane. This control permits optimizing the optical resonator for efficient coupling of the lowest order mode to the gain volume. This inherent flexibility is also required to convert the stable resonator described here to the stable–unstable resonator, which forms the basis of our high-power laser design [3]. The results of this paper therefore confirm the viability of the high-power design.

We also report results of a finite-element analysis of the thermal stresses in the slab. The analysis includes nonuniform heat deposition and cooling, temperature dependent thermomechanical properties, and temperature control of the bottom and top surfaces. We show that the thermal stresses are very poorly predicted by the uniformly pumped and uniformly side-cooled, high-aspect-ratio (slab height to the slab width) model that can be solved analytically.

Finally, we demonstrate efficient multimode and single transverse mode operation using the laser head.

II. LASER DESIGN

A cross-section of the laser head is shown in Fig. 1. The Nd:YAG slab is side-pumped from both sides by six fiber-coupled diode-laser bars. Each diode bar is coupled to 24, 250-μm core (275-μm outer diameter), 0.1 NA, step-index optical fibers. The fibers each supply 0.70 W of pump radiation, resulting in a total pump power of 100 W. The output wavelength of each diode laser is temperature tuned to the absorption peak
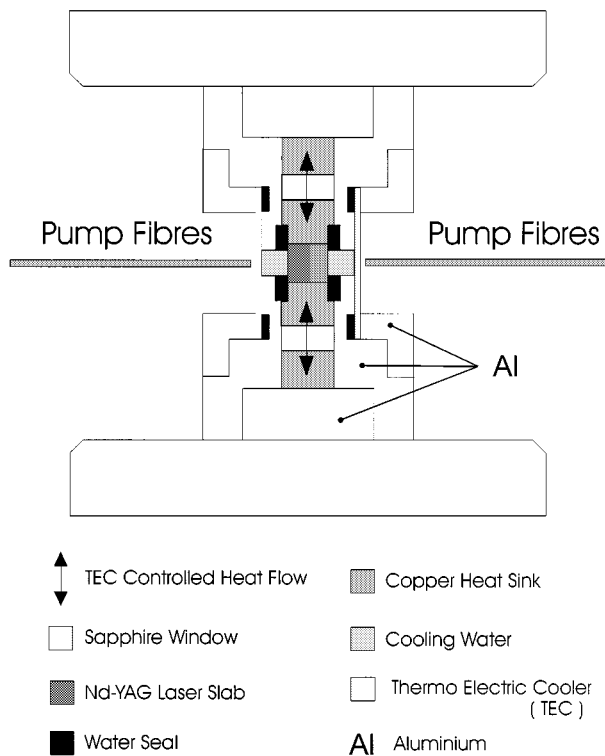
Fig. 1. Schematic diagram of the laser head geometry used to hold and cool the Nd:YAG laser crystal.

Fig. 2. Top view of the side-pumped, side-cooled TIR slab.

of Nd:YAG using individual servo-systems and thermoelectric coolers (TECs). The use of fiber-coupled diodes removes the diode lasers and their temperature control systems from the vicinity of the gain medium, thus reducing the complexity of the laser head [11]. Furthermore, the low numerical aperture of the fibers allows us to arrange the pumping to produce a high pump density without the need for complex focusing optics.

The Nd:YAG slab is side-cooled by water flowing along the sides of the crystal (flow direction orthogonal to the page in Fig. 1); the water channel is 1.5 mm high × 2 mm wide. A water flow of 320 ml/min. is used, which produces turbulent flow and thus provides better heat extraction.

The sides of the slab are coated with Teflon AF 1600[1] to prevent disruption of the total internal reflection (TIR) of the zigzag mode at the side faces by the gasket water seals [8]. A 4% Teflon: 96% FC-75 solution was used to coat the slab sides (FC-75 is the solvent for Teflon AF 1600).[2] With a refractive index similar to water and low absorption both at 808 nm and at 1064 nm, the Teflon coating does not disrupt the evanescent wave during TIR.

The pump light is transmitted through 0.5-mm-thick AR-coated sapphire windows, the cooling water, and the Teflon coating before it is incident on the Nd:YAG slab. The larger refractive indexes of these media decrease the divergence of the pump light, thus increasing the pump density. The pump density can easily be decreased by retracting the pump fibers away from the laser head.

Ideally, the heat generated by the pumping and the heat removal will be coplanar, and thus there will be only a weak thermal lens in the vertical direction. In practice, the vertical thermal lens has a focal length of 62 mm. However, the strength of the lensing can be reduced by using TECs shown in Fig. 1 (Marlow Industries SP1614) to heat the bottom and top surfaces of the slab [9]. The temperature of these surfaces is measured by a thermistor located in the copper heatsinks adjacent to the slab. The outermost heatsink is water "cooled." Indium foil is used to provide thermal contact between the slab, the heatsinks and the TECs.

Our folded zigzag configuration is a side-pumped, side-cooled version of a design developed by Richards and McInnes [12]. It has several advantages compared with other zigzag geometries. The width of the mode in the tangential (horizontal) plane is smaller for a given crystal width, which improves the dynamic stability of the resonator. Also, entry and exit of the mode at the same end of the slab facilitates the development of compact ring lasers [13], [14]. The slab has 19 TIR bounces and an angle of incidence $\theta_1 = 51°$ at the side faces of the slab (see Fig. 2). It has a parallel-side length of 34 mm (total length is 36.8 mm), a width of 3.0 mm, and a height of 3.4 mm.

III. THERMAL MODELING

The laser head described above is significantly different to the uniformly pumped, side-cooled, large-aspect-ratio geometry, the thermomechanical characteristics of which can be analyzed analytically. Such analytic models cannot easily include realistic pumping and cooling geometries, actual slab cross-sections, or temperature-dependent thermomechanical properties.

To better estimate the temperature and stress profile in the slab, we have developed an ANSYS[3] finite element analysis (FEA) model, which incorporates temperature-dependent thermomechanical properties. A brief summary of the main results is shown in Table I. Note that the stresses predicted by the "all inclusive" FEA model are much larger than those predicted by the analytic model.

The orientation of the coordinate system for the FEA model is shown in Fig. 3, and the parameters are listed in Table II. Since

[1]Teflon AF is an amorphous fluoropolymer developed by Du Pont Polymers.

[2]The authors gratefully acknowledge T. Rutherford and W. Tulloch of Stanford University, CA, for help with the application of Teflon to laser slabs.
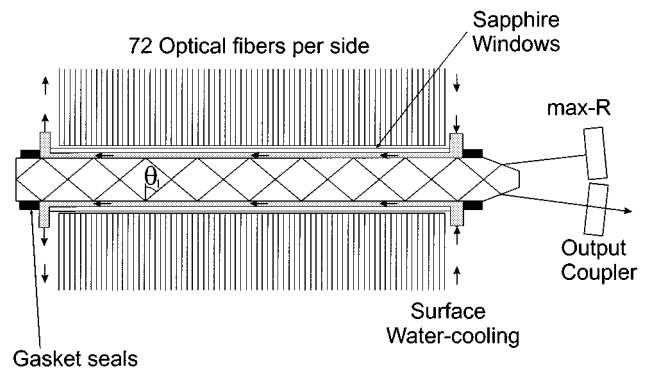
[3]ANSYS finite-element analysis package, version 5.5.3.

TABLE I
A SUMMARY OF THE MAXIMUM STRESS PREDICTED BY THE FEA MODEL AS
VARIOUS FEATURES ARE INCLUDED CUMMULATIVELY

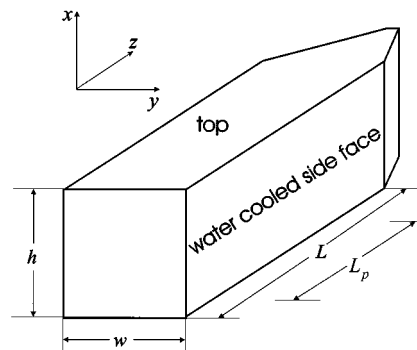| Features of model	Max. stress
Analytic model	15.2 MPa
FEA model	11.0 MPa
- include temp. dependence of k and α	21.7 MPa
- include realistic heat deposition	51.0 MPa
- include realistic side cooling	48.7 MPa
- include heating of bottom/top surfaces	44.2 MPa

Fig. 3. The coordinate system used for the thermal modeling. Note that the coordinate system is the same as that used in [7]. L_p is the length of the pumped section of the crystal.

TABLE II
ND:YAG PARAMETERS USED FOR FEA MODELING († MEASURED)

Parameter	Value
Absorption coefficient	4.1 cm^{-1} †
Fractional thermal load	0.241
Thermal conductivity (25°C), k	10.39 W/m.K [15]
Therm. exp. coeff. (25°C), α	6.9×10^{-6} K^{-1} [16]
Elastic modulus, E	282×10 GPa [17]
Specific heat, c_s	5.9×10^2 J/kg.K [18]
Poisson's ratio, ν	0.3 [15]
Thin film convection coefficient	1.8×10^4 W/m^2.K
Thermal power deposited, P_h	17 W
slab width, w	3.0 mm
slab height, h	3.4 mm
parallel side length of slab, L	34 mm
parallel side pumped length, L_p	22 mm

the length of the slab is much greater than its transverse dimensions, we assume that the plane strain approximation applies. Thus, the strain in the z-direction is zero [7] and our FEA model can be restricted to the crystal cross-section.

The pump power for this analysis is 100 W. The measured absorption coefficient at 808 nm is 4.1 cm^{-1}. Thus, a total of $P_h = 17$ W of heat will be deposited in the slab.

To validate the FEA model, we compared the predictions of the FEA and analytic models. The analytic model considers a slab that is infinitely long (z-direction) and high (x-direction), is uniformly pumped, is uniformly cooled on the sides, and has temperature-independent thermomechanical properties. It predicts that the stress in the y-direction is zero, $\sigma_{yy}(y) = 0$, due to the plane strain approximation. The stresses in x- and z-directions are identical, $\sigma_{xx}(y) = \sigma_{zz}(y)$. The maximum stress occurs at the side surfaces and is given by [7],

$$\sigma_{xx,\mathrm{max}} = P_h \frac{1}{12} \frac{\alpha E}{k(1-\nu)} \frac{w}{hL}. \qquad (1)$$

The symbols are defined in Table II. The maximum stresses predicted by the analytic and FEA models agree to within 0.2% for a slab that satisfies the assumptions of the analytic model.

Equation (1) predicts a maximum stress of 15.2 MPa for our slab. The maximum stress predicted by the uniformly pumped, uniformly cooled FEA model of our slab is 11.0 MPa.

Including the temperature dependance of the thermomechanical properties significantly increases the maximum stress in the slab, as has been noted by Brown [15], [16], [19], to 21.7 MPa. This increase is predominantly due to the temperature dependence of the thermal expansion coefficient α. The temperature dependence of α is included by using a polynomial fit to the data of Fan and Daneu [16] and Wynne *et al.* [19]. The temperature dependance of the thermal conductivity k is similarly included using the results of Brown [15]. The values of α and k at 25 °C are shown in Table II.

Another large increase in the predicted maximum stress occurred when a more realistic heat deposition was included. This assumed that the slab was illuminated by a Gaussian beam that initially diverged at a rate specified by the NA of the coupling fiber, was refracted at the interfaces through which it passed, and was then absorbed at a rate consistent with the measured absorption coefficient. Including the nonuniform heat deposition increased the predicted maximum stress to 51.0 MPa.

Nonuniform cooling of the side faces of the slab was also included, as the slab is cooled over only the central 1.5 mm. We assumed that the gasket water seal effectively insulates the upper and lower sections of the side faces. The heat deposition, temperature, and stress distributions are shown in Fig. 4. The predicted maximum stress with this cooling geometry is 48.7 MPa. While this stress is well below the fracture stress for Nd:YAG (280 MPa [17]), it is 320% larger than the stress predicted by the analytic model. Thus, it is essential to use the FEA model to estimate the stresses in the higher power lasers.

The maximum stress is only slightly affected by cooling or heating the bottom and top surfaces of the slab. The stresses were estimated by setting the temperatures of the bottom and top surfaces in the FEA model to those measured by the thermistors mounted in the copper heat sinks adjacent to these surfaces. The temperature distributions for maximum cooling and heating by the TECs are shown in Fig. 5. The maximum stress for cooling is 48.7 MPa and for heating is 44.2 MPa. Thus, heating of the bottom and top surfaces, as is required to reduce the strength of the vertical thermal lens (see Section IV), reduces the maximum stress.

IV. THERMAL LENSING

The strength of the thermal lens experienced by the zigzag mode was determined using a HeNe laser beam and a Mach–Zehnder interferometer. The Nd:YAG laser was lasing during this measurement since more of the energy in the upper state would otherwise be dissipated in the gain medium. This is due to an increased number of nonradiative transitions, thereby increasing the heating of the slab, and changing the boundary con-
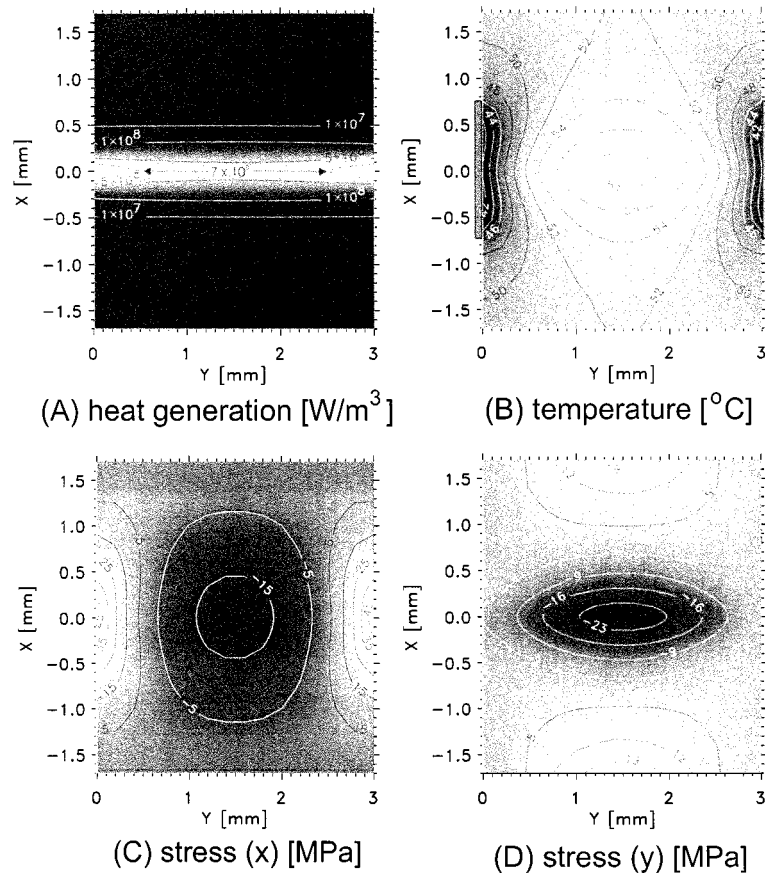
Fig. 4. Contour plots of the (A) heat deposition, (B) temperature, and (C), (D) stress distributions. The shaded rectangular boxes on the sides of (B) indicate the position of the water-cooling channels. The bottom and top surfaces of the slab were insulated. The maximum stress occurs in the x-direction at the center of the water-cooled side faces.
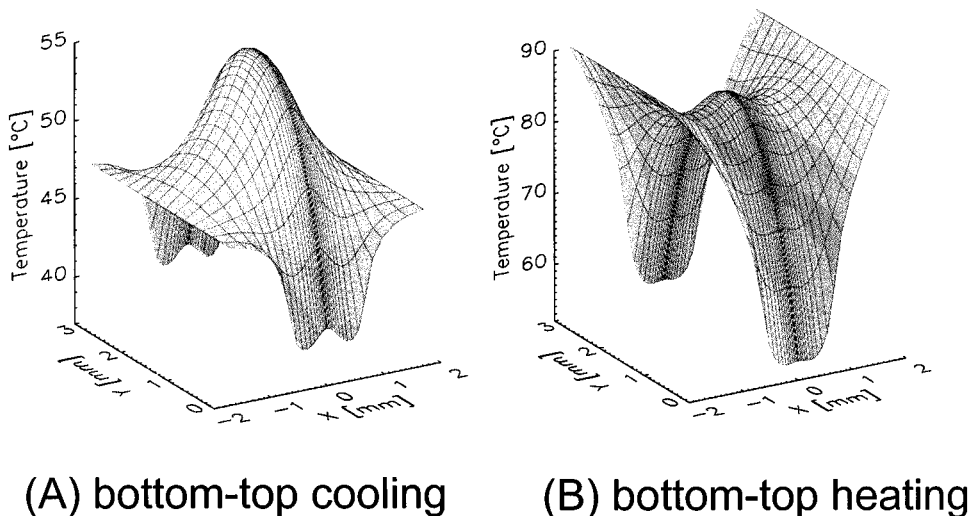

Fig. 5. Temperature profiles for 100-W pump power with the bottom/top TEC's operated at (A) maximum cooling and (B) heating.

ditions. Also the laser head would have absorbed photons from spontaneous emission.

The experimental setup is shown in Fig. 6. The size of the π-polarized HeNe laser beam is adjusted to fill the aperture of the Nd:YAG slab. The path of the HeNe beam within the slab follows the 19 TIR-bounce path of the laser mode. The interferometer arms have matched pathlengths. The Brewster window

of the slab closest to the charge-coupled device (CCD) is imaged onto the CCD. In the absence of pumping, the interferometer produced a "zero fringe" over the slab aperture. Laser operation was achieved with a short, multimode resonator.

Interferograms were recorded as the amount of heat deposited or removed by the TECs at the bottom and top of the slab was varied. The flow rate and temperature of the water used for the
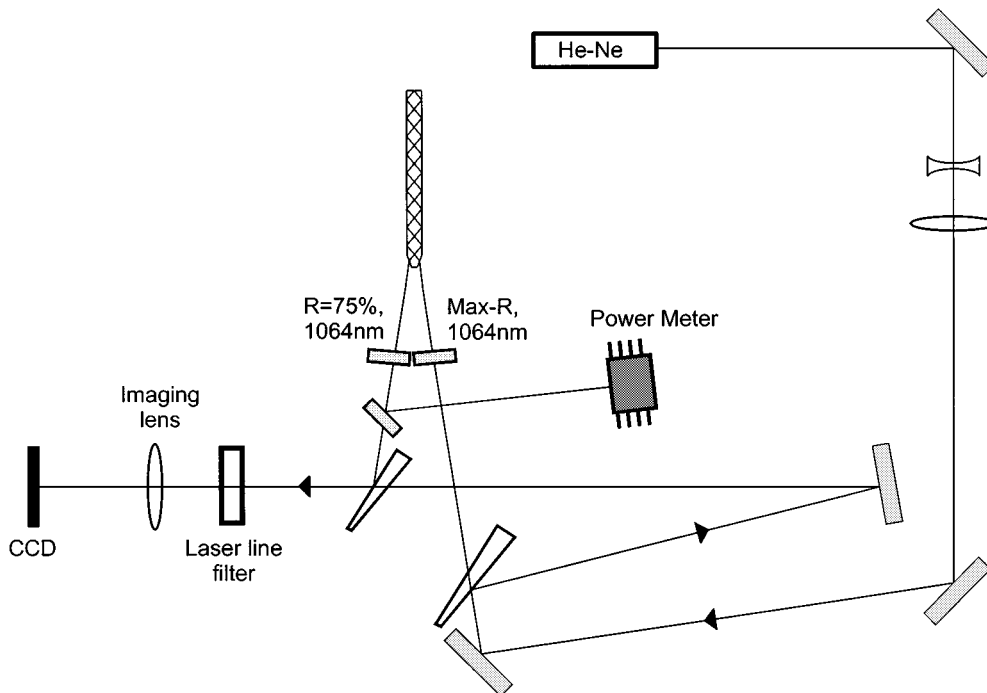
Fig. 6. A schematic diagram of the Mach–Zehnder interferometer used for the thermal lens measurement.

side cooling were constant. The interferograms are shown on the left-hand sides of Fig. 7(A)–(D). Note that heat removal (A) increases the number of fringes and thus the strength of the vertical thermal lens. Interferogram (B) corresponds to no active heat transfer by the TECs. Heating of the bottom and top surfaces reduces the vertical temperature gradient in the slab, (C), and a region of zero gradient is produced. As the heating is increased, the zero-gradient region migrates toward the center of the slab, as shown in (D). A further increase in heating would result in the formation of a negative lens in the central zone. These interferograms thus show that the vertical thermal lensing in the region of the laser mode can be adjusted by controlling the heat transfer through the bottom and top surfaces.

While the interferograms in Fig. 7 illustrate qualitatively the wavefront distortion by the laser head, quantitative analysis is difficult due to the limited number of fringes. Thus, the wavefront from the reference arm of the interferometer was tilted to increase the number of fringes, and a reference interferogram of the unpumped slab was recorded. The wavefront distortion due to the pumping of the slab was determined by subtracting the fringe positions in the reference interferogram from those in the interferograms of the pumped slab. The resulting profiles are shown on the right-hand sides of Fig. 7(A)–(D). As expected, cooling of the bottom and top surfaces increases the optical-pathlength gradient (A). Heating of these surfaces can reverse the gradient and reduce the wavefront distortion in the pumped region of the slab to less than ±0.1 of a wave (D). The strength of the thermal lens in the pumped region of the slab can be estimated by fitting a parabolic curve to the data and yields focal lengths of 47 (A), 66 (B), and 450 mm (D).

A similar analysis was performed for the horizontal plane. The wavefront distortion was less than ±0.2 of a wave, and was unchanged by the TEC operating conditions. Thus, the optical

design of the resonator in the horizontal plane will be independent of the vertical plane. The decoupling of thermal lensing is important for a scalable design.

V. LASER PERFORMANCE

A. Multimode

Multimode operation was achieved by placing two flat mirrors at normal incidence, 2 cm from the end of the crystal, in a configuration similar to that shown in Fig. 2. The bottom and top surfaces were cooled to allow higher order modes to oscillate and extract maximum power from the gain medium. The optimum reflectance of the output coupler was 75%, which resulted in a multimode output power of 32 W from 100 W of pump power. The multimode slope efficiency of the laser, with the TECs turned off, was 37%.

B. Single Transverse Mode

For single transverse mode operation, the mirrors were moved to 10.8 cm from the crystal end. Increasing the cavity length increased the diameter of the horizontal mode such that it efficiently filled the horizontal aperture created by the Brewster angled windows. This provided mode discrimination in the horizontal plane. In the vertical direction mode, discrimination was achieved with a combination of gain aperturing (only the central region of the crystal was pumped), increased armlength, and vertical thermal lens control accomplished by using the TECs to heat or cool the bottom and top of the slab.

Preliminary experiments have produced a laser power of 20 W with $M_y^2 = 1.19$ and $M_x^2 = 1.38$ with no thermal lens compensation. Heating the bottom and top of the crystal using the TECs with a current of −0.16 A improved the beam quality
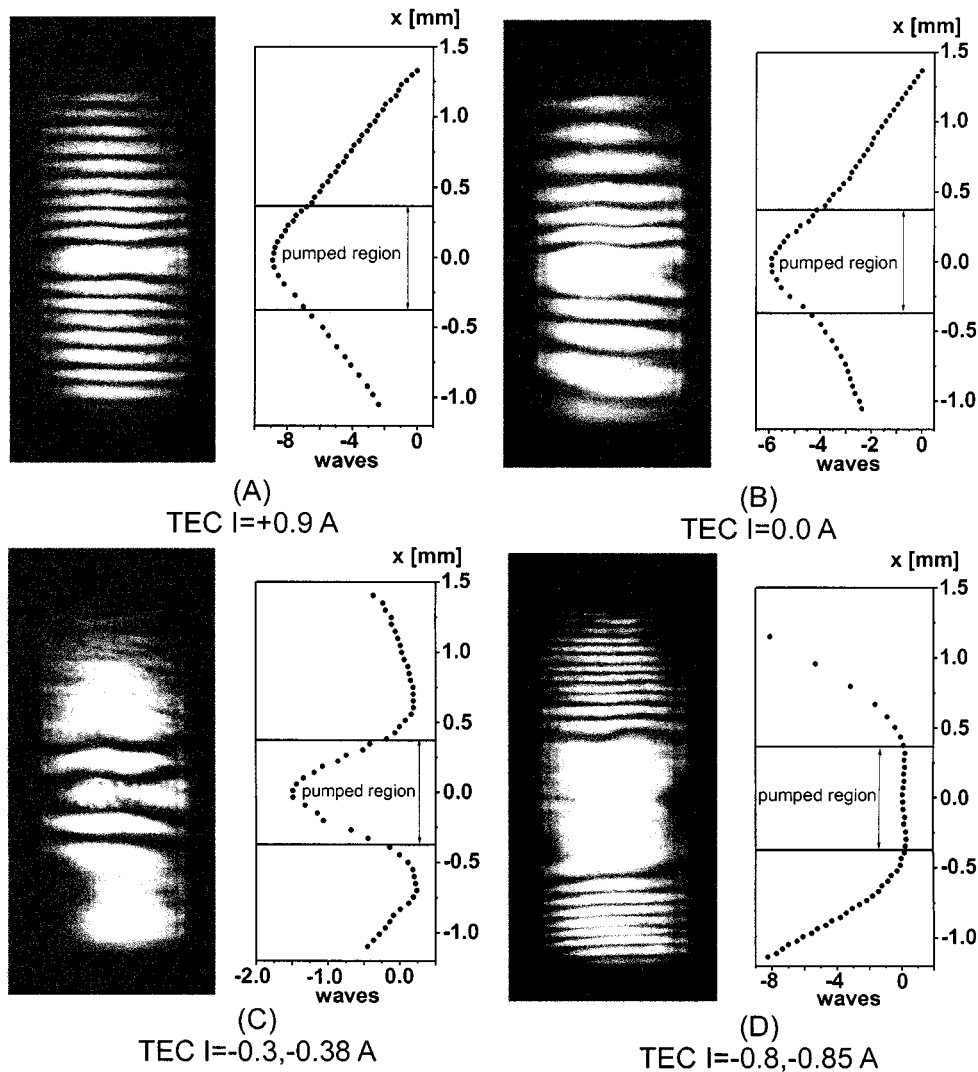
Fig. 7. Mach–Zehnder interferograms of the Nd:YAG slab crystal for different bottom and top TEC currents. Negative (positive) TEC currents correspond to heating (cooling). The deviations from zero-fringe are shown on the left-hand sides of (A)–(D). The data for the graphs on the right-hand sides of (A)–(D) was obtained by tilting the reference wavefront.

to $M_y^2 = 1.16$ and $M_x^2 = 1.15$ for 18.5 W of laser power. The pump power in both cases was 100 W.

VI. Conclusion

In order to produce a high-power scalable Nd:YAG laser, it is necessary to demonstrate control of the thermooptical and thermomechanical parameters. We have performed finite-element analyzes and subscale experimental investigations to verify that our high-power laser design, based on a diode-laser side-pumped, side-cooled Nd:YAG zigzag architecture is viable. During this process, we showed that the thermal lens in the vertical plane, normal to the zigzag, can be adjusted without changing the lensing in the zigzag plane. This permits an optimized design approach for a high-power laser using an unstable resonator. The decoupling of the weak horizontal thermal lens and the vertical thermal lens allows scaling of the mode volume in the vertical direction. Also, no increase, but rather a decrease, in the vertical thermal lens is expected when

scaling to higher powers. This is due to the improving match between the pumped and cooled areas of the slab, which occurs as the power is increased.

During this work, we also found that the FEA model described predicted stresses that were much higher than those predicted by simple analyzes, thus showing the importance of realistic estimates of the thermally induced stress in the crystal when scaling the power of slab lasers. We also demonstrated a compact, simple laser, which efficiently produced a near diffraction-limited TEM$_{00}$ output of 20 W when pumped with 100 W.

These results have greatly enhanced the viability of our high-power laser, designed for long baseline laser interferometric gravitational wave detection, which we are in the process of building.

References

[1] A. Giazotto, "Interferometric detection of gravitational waves," *Phys. Rep.*, vol. 182, pp. 367–424, 1989.

[2] A. Abramovici, W. Althouse, R. Drever, Y. Gursel, S. Kawamura, F. Raab, D. Shoemaker, L. Sievers, R. Spero, K. Thorne, R. Vogt, R. Weiss, S. Whitcombe, and M. Zucker, "LIGO: The interferometer gravitational-wave observatory," *Science*, vol. 256, pp. 325–333, 1992.

[3] D. Mudge, P. J. Veitch, J. Munch, D. Ottaway, and M. W. Hamilton, "High-power diode-laser-pumped CW solid-state lasers using stable-unstable resonators," *IEEE J. Select. Topics Quantum Electron.*, vol. 3, pp. 19–25, Feb. 1997.

[4] S. C. Tidwell, J. F. Seamans, and M. S. Bowers, "Highly efficient 60-W TEM$_{\circ\circ}$ cw diode-end-pumped Nd : YAG laser," *Opt. Lett.*, vol. 18, pp. 116–118, Jan. 1993.

[5] S. C. Tidwell, J. F. Seamans, M. S. Bowers, and A. K. Cousins, "Scaling CW diode-end-pumped Nd : YAG lasers to high average powers," *IEEE J. Quantum Electron.*, vol. 28, pp. 997–1009, Apr. 1992.

[6] D. Golla, M. Bode, S. Knoke, W. Schöne, and A. Tünnermann, "62-W cw TEM$_{\circ\circ}$ Nd : YAG laser side-pumped by fiber-coupled diode lasers," *Opt. Lett.*, vol. 21, pp. 210–212, Feb. 1996.

[7] J. M. Eggleston, T. J. Kane, K. Kuhn, J. Unternahrer, and R. L. Byer, "The slab geometry laser—Part I: Theory," *IEEE J. Quantum Electron.*, vol. 20, pp. 289–301, Mar. 1984.

[8] R. J. Shine, A. J. Alfrey, and R. L. Byer, "40-W cw, TEM$_{\circ\circ}$-mode, diode-laser-pumped, Nd : YAG miniature-slab laser," *Opt. Lett.*, vol. 20, pp. 459–461, Mar. 1995.

[9] R. J. StPierre, D. W. Mordaunt, H. Injeyan, J. G. Berg, R. C. Hilyard, M. E. Weber, M. G. Wickham, G. M. Harpole, and R. Senn, "Diode array pumped kilowatt laser," *IEEE J. Select. Topics Quantum Electron.*, vol. 3, pp. 53–58, Feb. 1997.

[10] R. J. StPierre, G. W. Holleman, M. Valley, H. Injeyan, J. G. Berg, G. M. Harpole, R. C. Hilyard, M. Mitchell, M. E. Weber, J. Zamel, T. Engler, D. Hall, R. Tinti, and J. Machan, "Active tracker laser (ATLAS)," *IEEE J. Select. Topics Quantum Electron.*, vol. 3, pp. 64–70, Feb. 1997.

[11] T. Y. Fan and R. L. Byer, "Diode laser-pumped solid-state lasers," *IEEE J. Quantum Electron.*, vol. 24, pp. 895–912, June 1988.

[12] J. Richards and A. McInnes, "Versatile, efficient, diode-pumped miniature slab laser," *Opt. Lett.*, vol. 20, pp. 371–373, Feb. 1995.

[13] D. J. Ottaway, P. J. Veitch, M. W. Hamilton, C. Hollitt, D. Mudge, and J. Munch, "A compact injection-locked Nd : YAG laser for gravitational wave detection," *IEEE J. Quantum Electron.*, vol. 34, pp. 2006–2009, Oct. 1998.

[14] D. J. Ottaway, P. J. Veitch, C. Hollitt, D. Mudge, M. W. Hamilton, and J. Munch, "Frequency and intensity noise of an injection-locked Nd : YAG ring laser," *Appl. Phys. B.*, vol. 70, pp. 1–6, June 2000.

[15] D. C. Brown, "Nonlinear thermal distortion in YAG rod amplifiers," *IEEE J. Quantum Electron.*, vol. 34, pp. 2383–2392, Dec. 1998.

[16] T. Y. Fan and J. L. Daneu, "Thermal coefficients of the optical path length and refractive index in YAG," *Appl. Opt.*, vol. 37, pp. 1635–1637, Mar. 1998.

[17] W. F. Krupke, M. D. Shinn, J. E. Marion, J. A. Caird, and S. E. Stokowski, "Sprectroscopic, optical, and thermomechanical properties of neodymium- and chromium-doped gadolinium scandium gallium garnet," *J. Opt. Soc. Amer. B*, vol. 3, pp. 102–114, Jan. 1986.

[18] W. Koechner, *Solid-State Laser Engineering*, 3rd ed, New York: Springer-Verlag, 1992.

[19] R. Wynne, J. L. Daneu, and T. Y. Fan, "Thermal coefficients of the expansion and refractive index in YAG," *Appl. Opt.*, vol. 38, pp. 3282–3284, May 1999.

D. Mudge, photograph and biography not available at the time of publication.

M. Ostermeyer, photograph and biography not available at the time of publication.

P. J. Veitch, photograph and biography not available at the time of publication.

J. Munch, photograph and biography not available at the time of publication.

B. Middlemiss, photograph and biography not available at the time of publication.

D. J. Ottaway, photograph and biography not available at the time of publication.

M. W. Hamilton, photograph and biography not available at the time of publication.